Article:
Casewell, S.L., Lawrie, K.A., Maxted, P.F.L. et al. (7 more authors) (2015) Multiwaveband photometry of the irradiated brown dwarf WD0137-349B. Monthly Notices of the Royal Astronomical Society, 447 (4). pp. 3218-3226. ISSN 0035-8711

https://doi.org/10.1093/mnras/stu2721

Monthly Notices
of the
ROYAL ASTRONOMICAL SOCIETY

MNRAS **447,** 3218–3226 (2015) doi:10.1093/mnras/stu2721

Multiwaveband photometry of the irradiated brown dwarf WD0137−349B

S. L. Casewell,[1⋆] K. A. Lawrie,[1] P. F. L. Maxted,[2] M. S. Marley,[3] J. J. Fortney,[4] P. B. Rimmer,[5] S. P. Littlefair,[6] G. Wynn,[1] M. R. Burleigh[1] and Ch. Helling[5]

[1]*Department of Physics and Astronomy, University of Leicester, University Road, Leicester LE1 7RH, UK*
[2]*Department of Physics and Astrophysics, Keele University, Keele, Staffordshire ST5 5BG, UK*
[3]*NASA Ames Research Center, MS-245-3, Moffett Field, CA 94035, USA*
[4]*Department of Astronomy and Astrophysics, University of California, Santa Cruz, CA 95064, USA*
[5]*SUPA, School of Physics and Astronomy, University of St Andrews, St Andrews KY16 9SS, UK*
[6]*Department of Physics and Astronomy, University of Sheffield, Sheffield S3 7RH, UK*

Accepted 2014 December 18. Received 2014 December 18; in original form 2014 July 21

ABSTRACT

WD0137−349 is a white dwarf–brown dwarf binary system in a 116 min orbit. We present radial velocity observations and multiwaveband photometry from *V*, *R* and *I* in the optical, to *J*, *H* and K_s in the near-IR and [3.6], [4.5], [5.8] and [8.0] μm in the mid-IR. The photometry and light curves show variability in all wavebands, with the amplitude peaking at [4.5] μm, where the system is also brightest. Fluxes and brightness temperatures were computed for the heated and unheated atmosphere of the brown dwarf (WD0137−349B) using synthetic spectra of the white dwarf using model atmosphere simulations. We show that the flux from the brown dwarf dayside is brighter than expected in the K_s and [4.5] μm bands when compared to models of irradiated brown dwarfs with full energy circulation and suggest this overluminosity may be attributed to H_2 fluorescence or H_3^+ being generated in the atmosphere by the UV irradiation.

Key words: binaries: close – brown dwarfs – white dwarfs.

1 INTRODUCTION

WD0137−349 is one of the only four known detached post-common envelope binaries containing a white dwarf and a brown dwarf companion. The other three are GD1400, (WD+L6, $P = 9.98$ h; Farihi & Christopher 2004; Dobbie et al. 2005; Burleigh et al. 2011), WD0837+185 (WD+T8, $P = 4.2$ h; Casewell et al. 2012) and NLTT5306 (WD+L4-L7, $P = 101.88$ min; Steele et al. 2013). Another eclipsing, candidate system has recently been reported (CSS21055; Beuermann et al. 2013) but is yet to be confirmed via radial velocity or spectroscopy.

WD0137−349 was discovered in 2006 by Maxted et al. (2006) and better characterized by Burleigh et al. (2006) using spectra from the Gemini telescope and the Gemini Near-InfraRed Spectrograph (GNIRS). The system is composed of a 0.4 $M_\odot$ DA white dwarf ($T_{\rm eff} = 16\,500$ K) and a secondary of mass 53 $M_{\rm Jup}$. The period of the system is 116 min and the estimated separation is 0.65 $R_\odot$ (Maxted et al. 2006). Burleigh et al. (2006) determined from the GNIRS spectra that an L8 is the most likely spectral type for the brown dwarf, and that it has not likely been affected by common envelope evolution. Such systems are not only important from an evolutionary point of view, giving us insight into the common envelope parameters (e.g. Casewell et al. 2012), but also provide insight into the properties of irritated atmospheres. WD0137−349B is a brown dwarf that intercepts ∼1 per cent of the light from its white dwarf companion. Due to the high effective temperature (16 500 K) of the white dwarf, this light is primarily in the ultraviolet regime. As the system is likely tidally locked, this means one side of the brown dwarf is continually irradiated by the white dwarf. This situation is similar to that in many exoplanets such as WASP-12b (Hebb et al. 2009) and HD 189733b (Knutson et al. 2012). Observing white dwarf+brown dwarf binaries have two advantages over similar exoplanet systems. The first is that brown dwarf atmospheres are well characterized (e.g. Cushing, Rayner & Vacca 2005), and that brown dwarf atmosphere modelling is more advanced than that of exoplanets. The second is that brown dwarfs are relatively bright so we can directly observe the brown dwarf in the *K* band and at longer wavelengths where the brown dwarf is brighter than its white dwarf companion (Burleigh et al. 2006; Maxted et al. 2006; Casewell et al. 2013).

2 OBSERVATIONS AND DATA REDUCTION

2.1 UVES spectra

We obtained 50 spectra of WD0137−349 through service mode observations made with the Ultraviolet and Visual Echelle

⋆ E-mail: slc25@star.le.ac.uk

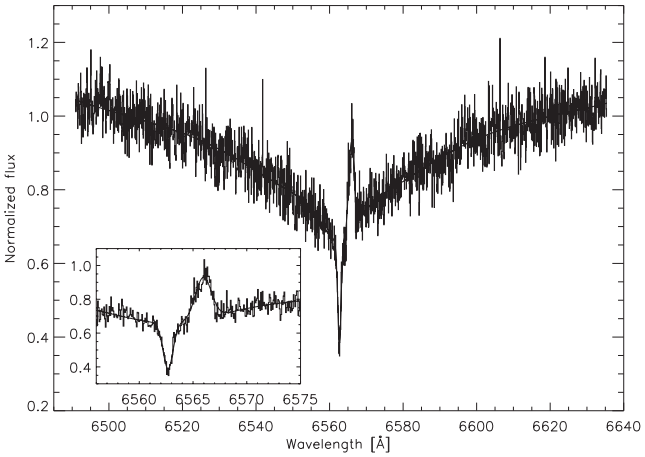

Figure 1. Least-squares fit to the Hα line for a typical UVES spectrum of WD0137−349. The observed spectrum is plotted as a histogram and the least-squares fit as a smooth line. Inset: detail showing the narrow core of the white dwarf absorption line and the emission line from the brown dwarf.

Spectograph (UVES) echelle spectrograph (Dekker et al. 2000) mounted on UT2 ('Kueyen') of the Very Large Telescope at the European Southern Observatory, Paranal, Chile (ESO programme ID 079.C-0683). We used a 1.4-arcsec-wide slit for these observations so the resolution of the spectra is set by the seeing. The ambient seeing during the exposures varied from 0.7 to 3.5 arcsec with a median value of 1.3 arcsec, corresponding to a resolution of 9.5 km s^{-1}. We used the CD4 cross-dispersing grating to observe the wavelength range 5655–9460 Å on the red arm. We do not use the blue arm data in this analysis. The exposure time was 240 seconds per spectrum. Spectra were reduced using the UVES pipeline version 4.3.0 provided by the observatory. The dispersion near the Hα line is 0.072 Å pixel^{-1} and typical signal to noise per pixel is about 20.

We also re-analysed the 20 UVES spectra reduced automatically at the observatory described in Maxted et al. (2006, ESO programme ID 276.D-5014). These spectra have an exposure time of 290 s and were obtained with the CD2 cross-dispersing grating, but are otherwise similar to the spectra described above.

We used the program MOLLY[1] to measure the radial velocities of the stars by fitting multiple Gaussian profiles to the Hα line. We used three Gaussian profiles with the same mean but independent widths to model the white dwarf absorption line and a single Gaussian profile for the emission line from the brown dwarf. Free parameters in the fit were the coefficients of a low-order polynomial used to model the continuum level, the depths of the two widest Gaussian profiles, the height of the Gaussian profile used to model the emission line from the brown dwarf and the positions of the emission and absorption lines. Other parameters for the Gaussian profiles were fixed at values determined from a preliminary least-squares fit. The least-squares fit to a typical spectrum is shown in Fig. 1. The radial velocities for the white dwarf and the emission line from the brown dwarf derived from these least-squares fits are given in Table 1.

We fitted a sine function of the form $V_r(\mathrm{WD}) = \gamma + K_{\mathrm{WD}} \sin(2\pi(t - T_0)/P)$ to the measured radial velocities of the white dwarf to determine the orbital period, P, and a reference time when the brown dwarf is at the furthest point in its orbit from the observer, T_0. We added 1 km s^{-1} in quadrature to the standard errors given in Table 1 in order to achieve a reduced chi-squared value for the fit $\chi^2_r = 1$. The parameters of this fit are given in Table 2. Also given in this table is a fit to the radial velocities measured for the emission line from the brown dwarf with the values of T_0 and P fixed to the values determined from the fit to the measured radial velocities of the white dwarf. We excluded measurements with large standard errors from this fit – these measurements come from spectra obtained at orbital phases where the emission line is very weak. To obtain $\chi^2_r = 1$ for the least-squares fit to the emission line radial velocities we had to add 5.5 km s^{-1} in quadrature to the standard errors given in Table 1. This much larger 'systematic error' is mostly the result of the variations in the shape of the line profile during the orbit that are not accounted for by fitting the line with a Gaussian profile. The fit to both sets of radial velocities are shown in Fig. 2.

[1] deneb.astro.warwick.ac.uk/phsaap/software

2.2 The optical imaging and its reduction

The optical data were observed using the South African Astronomical Observatory (SAAO) 1.0 m telescope and the SAAO CCD (STE3) instrument which has a CCD size of 512 × 512 pixels and a pixel scale of 0.31 arcsec pixel^{-1}. The observations are detailed in Table 3.

The data were reduced using the SAAO CCD pipeline which subtracted the bias and normalized the science frames with the master flat-field frame. We used the Starlink package AUTOPHOTOM to perform the photometry of the target and comparison stars. The aperture was fixed for the data and was set to be two times the mean seeing (full width at half-maximum; Naylor 1998). This aperture size limited the impact of the background noise in the aperture. The sky background level was determined using the clipped mean of the pixel value in an annulus around the stars and the measurement errors were estimated from the sky variance. To remove atmospheric fluctuations, the light curve was divided by the light curve of one of the comparison stars.

2.3 The near-IR imaging and its reduction

Photometry was obtained using Son OF Isaac (SOFI; Moorwood, Cuby & Lidman 1998) on the New Technology Telescope at La Silla on the nights of 2007-10-02 to 2007-10-04 and 2007-10-24 to 2007-10-26. The seeing was typically 1.5–2.0 arcsec, and the data were obtained in the J, H and K_s bands. The exposure times were 2 s in J, 4 s in H and 8 s in K_s, in a five-point jitter pattern which was then combined into mosaics to remove the sky background. The data were reduced using the Starlink package ORAC_DR with the SOFI-specific routines to perform the flat fielding, sky subtraction and mosaic combining. Object extraction was performed using aperture photometry routines within SExtractor and an aperture equivalent to the seeing.

To combine the K_s data from each night, each frame was calibrated using stars within the field from the 2 Micron All Sky Survey (Cutri et al. 2003). The J and H light curves are all from the same night. There are 130 points in the K_s-band light curve and 14 in the J and H light curves.

2.4 The *Spitzer* imaging and its reduction

We have also obtained *Spitzer* IRAC (Fazio et al. 2004) photometry from Cycle 7 (Programme ID:40325, PI: Burleigh) in all four bands ([3.6], [4.5], [5.8] and [8.0] μm). Each waveband was observed for one 116 min orbit. The data were observed using 30 s

Table 1. Radial velocity measurements for the white dwarf (V_r(WD)) and the emission line from the brown dwarf (V_r(em)) derived from multiple Gaussian profiles fit by least-squares to the Hα line.

HJD −2450000	V_r(WD) (km s^{-1})	V_r(em) (km s^{-1})	HJD −2450000	V_r(WD) (km s^{-1})	V_r(em) (km s^{-1})
3686.5258	10.6 ± 1.8	33.3 ± 3.4	4366.7203	32.8 ± 1.5	−79.1 ± 10.2
3686.5299	25.2 ± 1.5	−29.2 ± 2.7	4366.7238	21.6 ± 1.7	70.9 ± 21.6
3686.5339	30.7 ± 1.3	−86.3 ± 2.5	4366.7273	15.9 ± 1.9	28.4 ± 44.5
3686.5379	36.9 ± 1.2	−132.1 ± 2.3	4366.7308	10.1 ± 1.6	36.2 ± 24.6
3686.5420	43.0 ± 1.2	−163.6 ± 2.7	4366.7343	2.6 ± 1.4	135.3 ± 7.3
3686.5460	47.9 ± 1.2	−183.6 ± 3.1	4378.7497	−3.9 ± 1.0	146.6 ± 1.8
3686.5500	46.0 ± 1.2	−178.4 ± 3.5	4378.7532	2.9 ± 1.0	110.0 ± 2.0
3686.5540	40.3 ± 1.2	−161.4 ± 5.7	4378.7566	8.6 ± 1.2	56.2 ± 1.9
3686.5580	35.5 ± 1.2	−127.6 ± 8.0	4378.7600	18.8 ± 1.5	2.6 ± 2.3
3686.5621	28.7 ± 1.2	−84.2 ± 0.6	4378.7634	24.4 ± 1.1	−51.0 ± 1.8
3686.5661	20.7 ± 1.4	−10.3 ± 8.8	4378.7668	31.2 ± 1.0	−99.8 ± 1.8
3686.5701	11.6 ± 1.4	90.1 ± 9.4	4378.7702	37.1 ± 0.9	−140.2 ± 1.8
3686.5741	5.1 ± 1.2	121.0 ± 1.2	4378.7736	43.0 ± 0.9	−167.8 ± 2.0
3686.5782	−1.6 ± 1.2	149.1 ± 5.6	4378.7771	44.6 ± 1.0	−181.4 ± 2.4
3686.5822	−7.6 ± 1.1	170.9 ± 4.6	4378.7805	45.6 ± 1.0	−181.2 ± 2.5
3686.5862	−10.0 ± 1.1	190.9 ± 3.6	4387.6494	1.7 ± 1.2	101.8 ± 2.3
3686.5903	−9.5 ± 1.1	186.8 ± 2.9	4387.6528	6.8 ± 1.4	54.0 ± 2.1
3686.5943	−6.6 ± 1.1	174.3 ± 2.5	4387.6563	21.8 ± 2.0	7.4 ± 2.9
3686.5983	−0.8 ± 1.2	133.0 ± 2.6	4387.6597	24.5 ± 1.5	−52.7 ± 2.7
3686.6023	9.1 ± 1.4	78.6 ± 2.3	4387.6631	32.3 ± 1.3	−101.7 ± 2.5
4343.8265	44.8 ± 1.2	−180.2 ± 3.1	4387.6665	36.3 ± 1.4	−140.1 ± 2.6
4343.8299	44.5 ± 1.2	−186.4 ± 2.5	4387.6700	42.8 ± 1.3	−167.8 ± 2.7
4343.8333	45.5 ± 1.1	−177.4 ± 3.6	4387.6734	45.5 ± 1.3	−178.2 ± 3.3
4343.8367	43.9 ± 1.1	−158.1 ± 3.8	4387.6768	47.0 ± 1.3	−181.2 ± 4.9
4343.8401	37.9 ± 1.1	−137.0 ± 4.6	4387.6802	38.0 ± 1.8	−180.6 ± 6.4
4343.8436	34.3 ± 1.1	−118.5 ± 7.5	4400.5867	−10.0 ± 1.1	184.0 ± 2.8
4343.8470	27.2 ± 1.2	−56.1 ± 4.6	4400.5901	−3.4 ± 1.1	173.1 ± 2.4
4343.8504	21.0 ± 1.2	−63.2 ± 3.2	4400.5935	−1.0 ± 1.1	136.9 ± 2.1
4343.8538	10.6 ± 1.5	40.3 ± 2.4	4400.5969	6.6 ± 1.2	103.1 ± 2.4
4343.8572	4.8 ± 1.4	86.7 ± 1.5	4400.6004	7.7 ± 1.5	43.7 ± 2.3
4366.7030	46.6 ± 1.5	−183.5 ± 2.9	4400.6038	20.1 ± 1.6	−5.7 ± 2.5
4366.7064	42.8 ± 1.6	−189.4 ± 4.4	4400.6072	24.1 ± 1.3	−60.9 ± 2.5
4366.7099	43.9 ± 1.3	−174.4 ± 4.7	4400.6106	32.2 ± 1.1	−109.5 ± 2.4
4366.7134	40.8 ± 1.4	−150.3 ± 4.2	4400.6140	37.7 ± 1.1	−144.5 ± 2.3
4366.7168	35.3 ± 1.4	−134.1 ± 8.6	4400.6174	42.0 ± 1.1	−166.4 ± 2.1

Table 2. Parameters for least-squares fits of a circular orbit to our measured radial velocities, $V_r = \gamma + K \sin(2\pi(t - T_0)/P)$. Values in parentheses are standard errors on the final digit.

Parameter	White dwarf	Brown dwarf
T_0 (HJD)	2454178.6762(1)	–
P (d)	0.079 430 02(3)	–
γ (km s^{-1})	17.9(2)	3(1)
K (km s^{-1})	27.7(3)	−192(2)

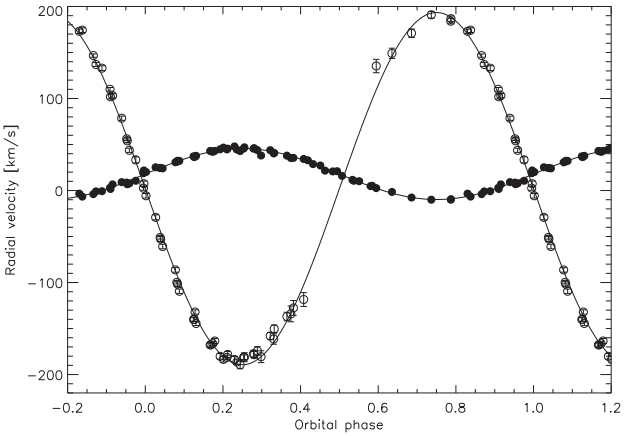

Figure 2. Least-squares fits of sine functions to the measured radial velocities of the white dwarf (filled circles) and the emission line from the brown dwarf (open circles).

integrations, the full array and no dithering, as time series photometry was required.

For the [3.6] and [4.5] μm data no additional processing was required and aperture photometry was performed on each individual image using the APEX software and an aperture of 3 pixels with a background aperture of 12–20 pixels. Pixel phase, array location dependence and aperture corrections were applied to the data and the IRAC zero magnitude flux densities as found on the *Spitzer* website were then used to convert the flux into magnitudes on the Vega magnitude scale. The photometric errors were estimated using the Poisson noise given by the APEX software which was then combined with the errors on the zero-points. The 3 per cent absolute calibration was added in quadrature to these photometric errors. The S/N of these data is typically 40.

For the [5.8] and [8.0] μm bands, the S/N was not high enough to perform aperture photometry on the individual images so the

Table 3. Observations from the SAAO.

Date	Filter	Number of points	Exposure time (s)	S/N
2007-11-28	*I*	29	200	100
2007-12-04	*V*	79	90	104
2008-11-08	*I*	322	42	70
2008-11-09	*R*	238	42	118
2008-11-10	*I*	137	42	79

recommended MOPEX pipeline (v18.3.6 final) was used to perform overlap corrections and to create final and array correction mosaics of the images, combining 20 images at a time resulting in a total exposure time of 600 s and S/N of 10–20. Aperture photometry was performed as for the [3.6] and [4.5] μm images. In total, we have 240 data points in the [3.6] and [4.5] μm bands, and 12 in the [5.8] and [8.0] μm bands.

3 RESULTS

We converted all of the UTC Julian dates in the image headers to BJD and fitted the *V*, *R* and *I* light curves to the ephemeris derived from the radial velocity measurements of the hydrogen absorption lines in the white dwarf. These are seen in Fig. 3. We fitted each night of data separately. The variability was determined by fitting a sine curve to the data. The peak-to-peak amplitude was measured to be 1.22 ± 0.3 per cent in *V*, 3.39 ± 0.23 per cent in *I* and 2.11 ± 0.15 per cent in *R* (Fig. 3). The light curve in the *I* band from 10-11-2008 has a peak-to-peak amplitude of 3.31 ± 0.33 per cent which is consistent with the data from 08-11-2008. The *I*-band light curve from 28-11-07 has a variability of 4.05 ± 0.51 per cent which is slightly larger than the other two nights of *I*-band data, but is still just within the errors. This light curve only has very few points (29) which do not cover a whole orbit of the system and a longer exposure time which means that the cadence of the data is not as good as for the other *I*-band data.

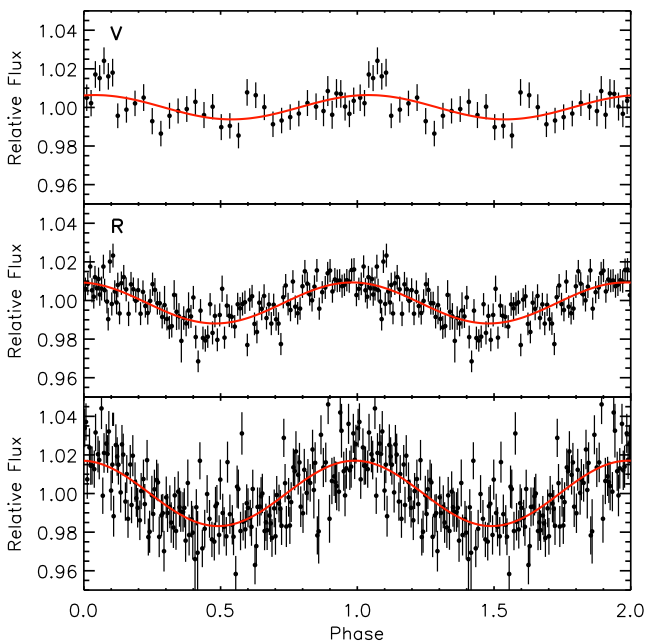

Figure 3. Two cycles of the *V*, *R* and *I* light curves of WD0137−349 folded on the ephemeris of the system (solid line), and binned by a factor of 2. Only the *I*-band data from 2008-11-08 are shown here.

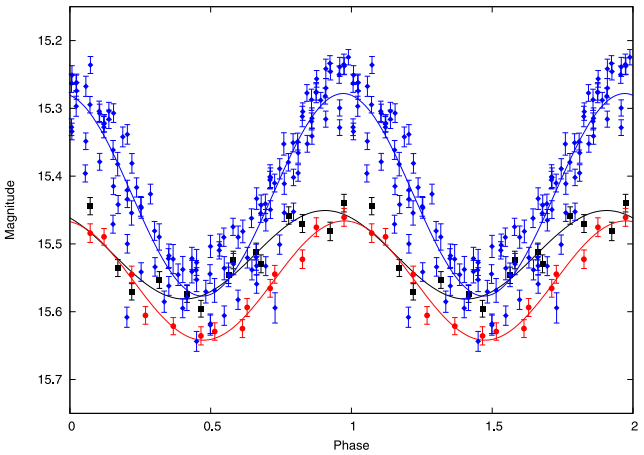

Figure 4. *J* (black squares), *H* (red circles) and K_s (blue diamonds) light curves of WD0137−349 folded on the ephemeris of the system.

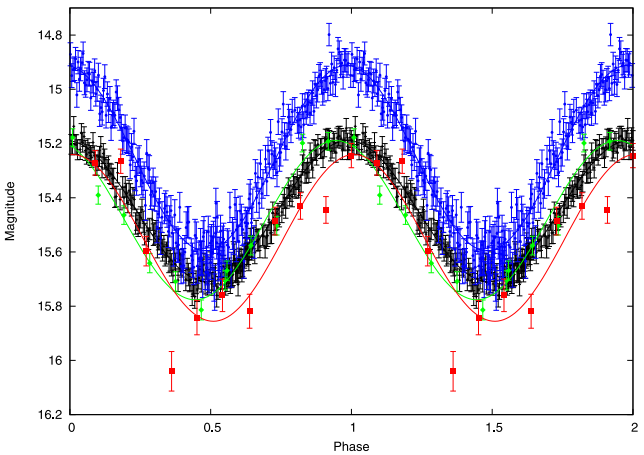

Figure 5. [3.6] (black +), [4.5] (blue circles), [5.8] (green diamonds) and [8.0] (red squares) μm light curves of WD0137−349 folded on the ephemeris of the system.

Table 4. Phase difference of light-curve fit compared to the ephemeris derived from the radial velocity.

Filter	Semi-amplitude	ϕ
J	0.06	0.064 ± 0.020
H	0.08	0.016 ± 0.009
K_s	0.15	0.004 ± 0.008
[3.6]	0.26	0.003 ± 0.002
[4.5]	0.34	0.009 ± 0.002
[5.8]	0.29	0.046 ± 0.010
[8.0]	0.31	0.076 ± 0.087

We fitted all of the near-infrared (Fig. 4) and mid-infrared (Fig. 5) data as above. All the photometry is in phase, and shows no statistically significant lag as is seen in Table 4. These data show that the irradiation is inducing a day/night contrast in the atmosphere of the brown dwarf. This is supported by the Hα detection.

To determine the brown dwarf flux, we generated a pure hydrogen white dwarf model using the plane-parallel, hydrostatic,

Table 5. Magnitudes and brightness temperatures of the combined white dwarf+brown dwarf system, the white dwarf magnitudes determined from the model and the irradiated and unirradiated hemispheres of WD0137−349B after the white dwarf has been subtracted. The errors on the brightness temperatures and flux reflect the error in the photometry and the uncertainty on the white dwarf temperature and gravity. We were unable to measure the nightside temperature in the *H* and [5.8] μm filters, and so an upper limit of the dayside flux has been used.

Waveband	Magnitude (WD+BD)		Magnitude (WD)	Magnitude (BD)		Brightness temperature (K)	
	Dayside	Nightside		Dayside	Nightside	Dayside	Nightside
J	15.45 ± 0.01	15.59 ± 0.01	15.72 ± 0.12	$17.14^{+0.42}_{-0.84}$	$17.97^{+0.87}_{-3.39}$	2418^{+201}_{-329}	2085^{+287}_{-769}
H	15.47 ± 0.01	15.65 ± 0.01	15.52 ± 0.12	18.33 ± 0.80	18.33	1585 ± 329	1585
K_s	15.28 ± 0.01	15.57 ± 0.01	15.77 ± 0.12	16.37 ± 0.29	$17.49^{+0.56}_{-1.16}$	2015^{+119}_{-131}	1537^{+183}_{-262}
[3.6]	15.19 ± 0.04	15.71 ± 0.04	15.82±0.12	$16.03^{+0.34}_{-0.17}$	$18.04^{+1.49}_{-0.82}$	1668^{+103}_{-110}	958^{+184}_{-508}
[4.5]	14.91 ± 0.04	15.60 ± 0.06	15.85 ± 0.12	$15.50^{+0.19}_{-0.15}$	$17.31^{+1.10}_{-0.61}$	1808^{+91}_{-93}	974^{+138}_{-180}
[5.8]	15.19 ± 0.03	15.78 ± 0.04	15.76 ± 0.12	$16.12^{+0.43}_{-0.16}$	16.12	1254^{+97}_{-101}	1254
[8.0]	15.85 ± 0.06	15.24 ± 0.05	15.82 ± 0.12	$16.06^{+0.59}_{-0.1}$	19.88 ± 2.2	1102^{+99}_{-102}	364 ± 249

non-local thermodynamic equilibrium (non-LTE) atmosphere and spectral synthesis codes TLUSTY (Hubeny 1988; Hubeny & Lanz 1995) and SYNSPEC (Hubeny & Lanz 2001) for an effective temperature of 16 500 K and log *g* of 7.49 (Maxted et al. 2006). We then convolved this spectrum with the filter profiles from 2MASS and IRAC, to get the total white dwarf flux per filter. These flux measurements, including a 12 per cent error to take into account the error in the effective temperature (500 K) and log *g* (0.08) as in Maxted et al. (2006), were then compared to the theoretical colour tables for white dwarfs (Holberg & Bergeron 2006; Kowalski & Saumon 2006; Tremblay, Bergeron & Gianninas 2011) which have been extended into the *Spitzer* bandpasses (Bergeron, private communication) and were also found to be consistent. The total white dwarf flux per filter was then subtracted from the observed flux (white dwarf + brown dwarf combined) at the maximum and minimum values. This flux value was then converted back into magnitudes (Table 5).

It is evident from this calculation that we do not detect any flux from the nightside of the brown dwarf in the *H* or [5.8] μm wavebands, and the values for the dayside of the brown dwarf have been used as upper limits. This is based on the assumption that the nightside cannot be brighter than the dayside. Using the magnitudes from Table 5, we calculated the brightness temperature at each wavelength from the *J* band to [8.0] μm on the heated and unheated side of WD0137−349B and they can also be seen in Table 5 and Fig. 7. These temperatures seem to imply that there is a weak dayside temperature inversion between the scaleheights probed in the K_s and [4.5] μm bands. This is not uncommon in hot Jupiter atmospheres and is normally attributed to the presence of TiO/VO opacity (Hubeny, Burrows & Sudarsky 2003; Fortney et al. 2008).

In Burleigh et al. (2006), we estimated the equilibrium temperature of the irradiated side of WD0137−349B. The equilibrium temperature is the temperature of the heated side if the white dwarf and brown dwarf are perfect black bodies and is calculated to be ∼2000 K. This is too hot for an L6 dwarf, but this estimate is broadly consistent with our brightness temperature calculations. While fig. 2 of Casewell et al. (2013) shows that *JHK* photometry of the heated face of the brown dwarf is consistent with an L6 dwarf, it is likely that there are other mechanisms occurring within the brown dwarf atmosphere, particularly considering that while one hemisphere is being irradiated, energy is being redistributed around the object as has been suggested for some exoplanets (e.g. Cooper & Showman 2005).

4 MODELLING THE DATA

The likely atmospheric circulation and irradiation of WD0137−349B make it unreasonable to compare the photometry of WD0137−349B with that of unirradiated brown dwarfs, as had been done in the past (Burleigh et al. 2006). Therefore, we have used models that take into account the high level of UV irradiation in this system and use them to explore the heat transport and potential temperature inversion as well as the effects of some photochemistry.

4.1 The irradiated hemisphere

To explore the response of a brown dwarf atmosphere to the intense irradiation environment and to explore the possibility of a temperature inversion, we computed a few exploratory models using the atmospheric structure model of Marley et al. (1999), Marley et al. (2002) and Fortney et al. (2005) with a log $g = 5.32$ surface gravity and intrinsic effective temperatures ranging from 600–1000 K. The choice of intrinsic effective temperature does not affect the results as in all models the incident flux dominates the energy budget and is far larger than the intrinsic flux. The white dwarf parent star has a $T_{\rm eff}$ =16 500 K, placing the peak of its Planck function well into the UV. The model atmosphere code we use for the brown dwarf, which was generally developed for Sun-like stars, lacks opacities at such short wavelengths. To model the incident flux, we instead used a cooler 10 000 K blackbody with a larger white dwarf radius such that same total incident flux, but peaking at a longer wavelength, was maintained for the brown dwarf at 0.003 au. The temperature–pressure profiles are shown in Fig. 6. As is common for hot Jupiters (e.g. Fortney et al. 2006), we explored two cases for re-radiation of the absorbed flux on the irradiated atmosphere. In some models, the incident flux is cut by one-half, to simulate energy being efficiently lost to the unmodelled nightside (full circulation models). In others, the full incident flux is used, to simulate no energy lost to the nightside, which leads to a hotter dayside model. Our aim was not to reproduce the observed photometry but rather to understand the type of response that would be expected in radiative–convective and thermochemical equilibrium. As is also customary for irradiated hot Jupiter models, we considered cases in which the brown dwarf's atmosphere both contained and lacked gaseous TiO. Since TiO absorbs strongly at optical wavelengths, it has been suggested as the absorber responsible for creating atmospheric thermal inversions in some hot Jupiters (Hubeny et al. 2003; Fortney et al. 2008).

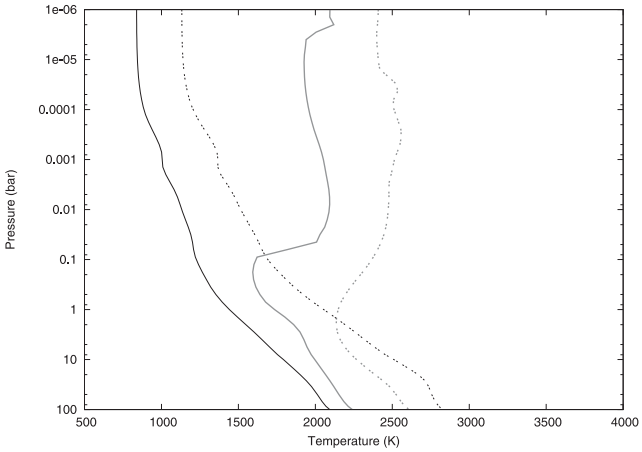

Figure 6. The temperature–pressure profiles for the dayside of the irradiated brown dwarf model. Solid lines are models that use full circulation and energy transport from the heated to non-heated side of the brown dwarf. Dotted lines show the zero circulation models. The grey lines are models containing TiO and black lines for the non-TiO model.

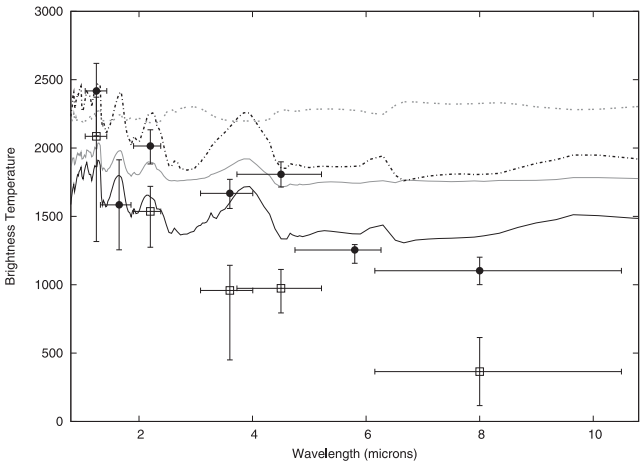

Figure 7. Brightness temperatures for WD0137−349 on the irradiated (circles) and unirradiated (open boxes) sides of the brown dwarf. The *H* and [5.8] temperatures for the unirradiated side are upper limits only (diamonds), derived from the white dwarf's flux. The error bars on the *X*-scale represent the widths of the filters used. The models are as for Fig. 6 and show the dayside only.

Model brightness temperature spectra for these cases are shown in Fig. 7.

It is clear that the models with the full circulation, where energy is being lost to the nightside, produce brightness temperatures closer to those observed. The data also show a larger dayside brightness temperature for the K_s band than for [4.5] μm. Since the opacity is larger in the former bandpass than the latter, this implies a temperature profile that increases with altitude above a minimum. The difference is relatively small, ∼200 K, but is similar to that seen in exoplanets (e.g. Madhusudhan et al. 2011). Surprisingly, however, the overall flux levels are better matched by the models lacking in TiO, which raises a question as to which absorber would then be responsible for the inversion. Furthermore, the condensation temperature of TiO is ∼1670 K, therefore in WD0137−349B, TiO (and the similar VO) should be present in the atmosphere.

Two explanations for this unexpected behaviour seem likely. First, it is possible that when WD0137−349B orbited the white dwarf progenitor that the TiO and VO condensed out of the upper atmosphere. The nightside photometry indicates that it may have had an effective temperature of 1000 K, cool enough for condensation to occur. It is also possible that the temperature inversion is not real, and that the greater brightness temperature at K_s is in fact due to overluminosity caused by photochemistry which is not included in these models.

The *J* band also appears anomalously high, but it can be seen from the spectra in Casewell et al. (2013) and Burleigh et al. (2006) that the brown dwarf is contributing very little of the flux at these wavelengths, and what we are likely detecting is scattered light off the brown dwarf atmosphere. Despite the majority of the incident light from the white dwarf being emitted in the UV, it is unlikely that we will see some sort of photochemical haze as predicted by Zahnle, Marley & Fortney (2009) as these should dissipate at effective temperatures greater than 1000 K. It is possible, however, that we are seeing some form of airglow such as the H_3^+ seen at Jupiter (Drossart et al. 1989), Saturn (Trafton et al. 1993) and Uranus (Geballe, Jagod & Oka 1993) which emits at wavelengths between 2 and 6 μm, and is strongest between 3 and 5 μm (Neale, Miller & Tennyson 1996, calculated as part of the exomol project Tennyson & Yurchenko 2012) at the temperature and pressure of a mid-L dwarf. Another possibility for the overluminosity is that we see H_2 fluorescence as was recently detected in the UV active M dwarf exoplanet hosts (France et al. 2013). However, it has not been determined whether the fluorescence is due to the M dwarf activity, or the irradiation of the planet.

4.2 Photochemistry

We utilize the temperature–pressure profile for the dayside of the irradiated brown dwarf model without TiO, using full convection and energy transport (the solid black line in Fig. 6). The ion–neutral chemistry of Rimmer, Helling & Bilger (2014) is applied on top of this temperature–pressure profile non-self-consistently, with the photochemistry from Yelle (2004, and references within). Rate coefficients for photolysis due to the irradiating white dwarf are calculated by assuming that the white dwarf produces a UV field as a blackbody with $T_{\rm irr} = 16\,500$ K. The UV field is attenuated by H_2 self-shielding, using shielding coefficients given by Lee et al. (1996). The number densities of H, H_2 and H_3^+ are shown on top of the pressure–temperature profile in Fig. 8.

The molecular hydrogen in the upper atmosphere of a brown dwarf in the presence of a strong UV field produced by a nearby white dwarf may become excited by absorbing photons in the lines of the $B^1\Sigma_u - X^1\Sigma_g^+$ and $C^1\Pi_u - X^1\Sigma_g^+$ bands. These molecules will rapidly transition into either the continuum ground-state, resulting in dissociation (Field, Somerville & Dressler 1966), or will find themselves within the rovibrationally excited ground state. Molecular hydrogen in these excited states will be spontaneously de-excited into states progressively closer to the ground state. We determine the line intensity for IR fluorescence lines for rovibrationally excited H_2 within its electronic ground state, using Sternberg & Dalgarno (1989):

$$F_\nu(v'j' \rightarrow vj) = \frac{h\nu}{4\pi} N(v'j') A(v'j' \rightarrow vj) g(\nu - \nu_0), \quad (1)$$

where ν_0 [Hz] is the transition frequency, $N(v'j')$ [cm^{-2}] is the column density of the excited species, A [s^{-1}] is the rate of the transition from $v'j' \rightarrow vj$ and $g(\nu - \nu_0)$ is the line-shape, which we assume to be susceptible to Doppler broadening only. The value of $N(v'j')$ can be determined as in equation 2 from Sternberg & Dalgarno (1989),

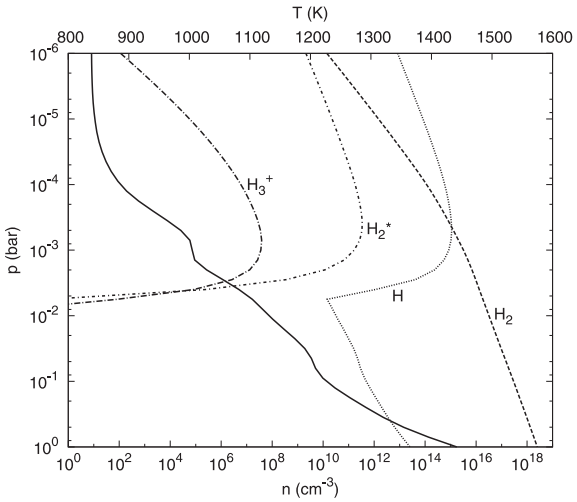

Figure 8. The number densities [cm^{-3}] of H, H_2 and H_3^+ and UV-pumped H_2 (denoted by H_2^*, bottom *x*-axis) as a function of pressure [bar] (*y*-axis), as calculated by applying the chemical network of Rimmer et al. (2014) to the (non-TiO) temperature–pressure profile of 6. The temperature–pressure profile used is shown here as a sold line (gas temperature [K] in the top *x*-axis).

using H_2 formation via three-body reactions (Baulch et al. 1994). A unitless scaling parameter in this set of equations, χ, represents the strength of the UV field at ∼100 nm, and is given in Draine units (Draine 1978). The value of χ is parametrized by Sternberg & Dalgarno (1989, their equation A7):

$$\chi = 3600 \left(\frac{R}{R_\odot}\right)^2 \left(\frac{r}{1\ \mathrm{pc}}\right)^{-2} \frac{1}{e^{14.4/T_4} - 1}, \quad (2)$$

where T_4 is the temperature of the white dwarf in units of 10^4 K, R is the radius of the white dwarf in units of solar radii and r is the distance between the white dwarf and brown dwarf in units of parsecs. For WD0137, $T_{\rm eff} = 16\,500$ K, $R/R_\odot \approx 0.019$ and $r \approx 1.8 \times 10^{-6}$ pc. This yields an enormous value of $\chi = 6.5 \times 10^7$. A strong UV flux means that the rovibrational states of the molecular hydrogen will be highly populated; however, if the field is very high, the dissociation rates will also be large, and most of the hydrogen will be atomic. Because of the self-shielding of molecular hydrogen, the UV pumping will nevertheless become efficient. When χ is large, H_2 fluorescence will become significant deeper in the brown dwarf atmosphere. For $\chi \sim 10^7$, self-shielding does not become effective at protecting the molecular hydrogen until ∼1 mbar for our model atmosphere. The number density of UV-pumped H_2, $n(H_2^*)$ [cm^{-3}], is shown in Fig. 8.

4.2.1 H_3^+ emission

The molecular hydrogen can also be ionized by energetic particles and UV photons, forming H_2^+, which then reacts with molecular hydrogen to form H_3^+. In the presence of strong external radiation, the gas in the upper atmosphere of the brown dwarf will become weakly ionized, and we assume that free electrons will dominate the destruction of H_3^+. The H_3^+ abundance is solved using the chemical kinetics network, albeit not self-consistently. Most importantly, the atmospheric dynamics from the model brown dwarf atmosphere are not coupled to the chemistry, and the effect of H_3^+ radiative cooling is not coupled to the thermal balance of the model atmosphere.

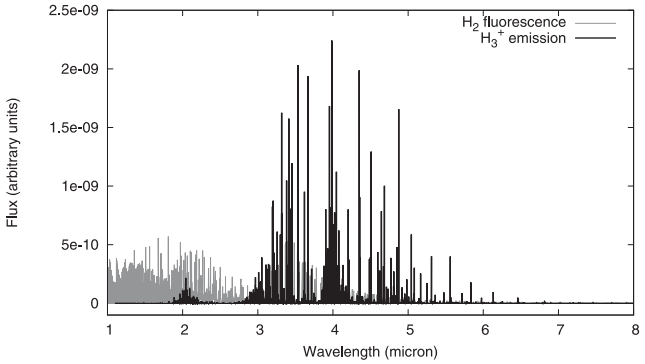

Figure 9. H_2 fluorescence (grey) and H_3^+ emission (black) spectra for WD0137−349B. The flux scale is in relative units, as we cannot calculate exactly how much emission would be expected without having models that fully incorporate photochemistry, the coupling to the thermal structure and the atmospheric dynamics. Additionally, the Sternberg & Dalgarno (1989) approximation for the H_2 fluorescence has not been tested for high densities as yet. We will address these issues in a future publication.

Within these limitations, the chemistry calculations predict that the majority of H_3^+ is between 10^{-6} bar (the low pressure limit of the model atmosphere), and 10^{-2} bar, with a peak abundance of 10^8 cm^{-3} (about 100 times the peak abundance observed on Jupiter; see Melin et al. 2005, their fig. 1). When we calculate the line profile, we assume all the emitting energy levels are in LTE, for simplicity; we take for our H_3^+ cross-sections the Exomol data base values (Neale et al. 1996; Hill, Yurchenko & Tennyson 2013). Eventually, non-LTE models should be used, but LTE models are commonly used to model H_3^+ in Jupiter (Miller et al. 2000) and non-LTE models suggest that, at least for Jupiter, the assumption of LTE for emitting energy levels accurately reproduces the overall emission rate of H_3^+ (Melin et al. 2005). This assumption is sufficient for our purposes here.

Both the modelled H_3^+ and H_2 emission spectra are shown in Fig. 9.

5 DISCUSSION

WD0137−349B clearly has a large temperature difference between the irradiated and non-irradiated hemispheres. This difference is largest in the [4.5] μm band at 834 K, and is 710 K at [3.6] μm and 478 K in K_s, and the errors on these measurements are 89, 400 and 143 K; although as these errors are strongly correlated with the errors on the white dwarf $T_{\rm eff}$ and log g, they may be an overestimate. The error on the [3.6] μm band is large, due to the uncertainty associated with the minimum nightside flux. In contrast, the exoplanet HD 189733b has brightness temperatures of 1328 K in [3.6] and 1192 K in [4.5] μm, and a difference in day and nightside temperatures of 503 K at [3.6] μm, and 264 K at [4.5] μm (Knutson et al. 2012). WASP-12b is one of the most highly irradiated exoplanets and is estimated to have a 3000 K dayside and a 1100 K nightside (Sing et al. 2013). While the temperature differences are not as extreme as for WASP-12b, WD0137−349B is hotter than HD 189773b on the dayside and colder on the nightside.

Despite searches, there have been no detections of H_3^+ in either exoplanets or brown dwarfs to date (e.g. Goto et al. 2005). However, France et al. (2013) have reported detections of H_2 fluorescence in planets around M dwarfs. This H_2 is detected in the Lyman α line in the UV. However, despite detecting the emission

in four of the six M dwarf planetary systems studied, they are unable to confirm whether the H_2 has a chromospheric origin or is being emitted from the planet itself. It is evident that more detailed modelling is required, particularly in the UV wavelengths to predict whether H_2 is detectable within Lyman α in a white dwarf spectrum.

Lammer et al. (2003) argue that while H_3^+ is a common molecule that cools the thermosphere of planets such as Jupiter (Miller et al. 2000), it may not have the same effect in exoplanets as those orbiting within 0.1 au of their host star will reach temperatures high enough to dissociate H_2 ($\sim$ 10 000 K), preventing its formation. This dissociation is also caused by the high UV irradiation at these close separations. Koskinen et al. (2007) claim that this is not entirely correct, as Lammer et al. (2003) neglected the cooling effect that H_3^+ produces, arguing instead that the presence of H_3^+ can cool the atmospheres enough to generate more H_3^+. Yelle (2004) produced similar calculations and using 1D models determined that in some hot Jupiters the thermosphere can reach 10 000–15 000 K and still have cooling provided by H_3^+ at lower altitudes in the thermosphere, even though the H_2 is rapidly lost via thermal dissociation. Indeed, these models show that H_3^+ cooling has a significant impact on the temperature profiles of close-in exoplanets in spite of the low density of H_3^+ in the thermospheres of these exoplanets, compared to the H_3^+ densities in the Jupiter's ionosphere.

Koskinen et al. (2007) get a slightly different result and also include radiative cooling and atmospheric circulation in their models. They note that dissociation occurs at a much lower 3000 K on a planet around a solar-type star at $\sim$0.1 au. While WD0137−349B has a separation of 0.003 au, the brightness and equilibrium temperatures are much lower than 3000 K, because the white dwarf luminosity is lower than that of a solar-type star.

There are a handful of brown dwarfs known to be irradiated by stellar companions (e.g. WASP-30B, Anderson et al. 2011; Kelt-1b, Beatty et al. 2014); however, their equilibrium temperatures are in general too high to harbour H_3^+. For example, Kelt-1b (Beatty et al. 2014). It is estimated to have an brightness temperature of $\sim$3000 K at [3.6] and [4.5] μm on the dayside, with a tentative detection of a temperature inversion suggesting a nightside cold trap indicating temperatures of $\sim$2000 K. It orbits within 0.1 au making H_3^+ formation unlikely. This is supported by the [3.6]–[4.5] colour, which they note is identical to that of an isolated brown dwarf of similar temperature.

While Burleigh et al. (2006) compared their nightside spectrum of WD0137−349B with a combined model of a white dwarf and an L8 dwarf in the near-IR, the *H*-band flux is much lower than this. This inconstancy seems to indicate that in the mid-IR, a significant departure from a canonical brown dwarf spectrum is seen. This change is possibly due to energy transport around the brown dwarf from the heated to the unheated hemisphere. The measurements of the heated side, however, do not seem to indicate a temperature inversion due to TiO as is seen in some exoplanets, but instead suggests a possible brightening in the *K* and [4.5] μm bands, possibly due to H_3^+ and H_2 fluorescence.

Phase resolved spectra of WD0137−349B in the *K* band will allow some determination of how the spectrum alters with phase and whether species such as H_3^+ and effects such as H_2 fluorescence are occurring. *L*- and *M*-band spectroscopy from Mid-Infrared E-ELT Imager and Spectrograph (METIS) on European Extremely Large Telescope (E-ELT) or Near-Infrared spectrograph (NIRSpec) from *JWST* could also be used confirm this effect. It is also clear that models of irradiated brown dwarfs and exoplanets need to be extended to include photochemistry and fluorescent effects.

6 SUMMARY

We have observed the detached post-common envelope white dwarf+brown dwarf binary WD0137−349 in all four *Spitzer* IRAC bands, obtaining an orbit at each wavelength as well as in the optical *R*-, *I*- and *Z*-optical wavebands. Variability on the 116 min orbit is seen at all wavelengths. The trend presented in Casewell et al. (2013) in which the aptitude of the peak-to-peak variability increases with wavelength is continued until 4.5 μm, after which the variability drops and remains constant. We calculate brightness temperatures and magnitudes for the brown dwarf alone and suggest that the tentative detection of a temperature inversion (based on brightness temperatures) is possibly not real and may be due to some other effect such as the UV irradiation of WD0137−349B creating photochemical effects in the atmosphere. These species are most luminous in the K_s and [4.5] μm bands, thus potentially giving the appearance of a temperature inversion.

ACKNOWLEDGEMENTS

We thank Derek Homier for his useful comments at the refereeing stage. SLC acknowledges support from the College of Science and Engineering at the University of Leicester. PBR and ChH highlight financial support of the European Community under the FP7 by an ERC starting grant. SPL is supported by STFC grant ST/J001589/1. This work is based [in part] on observations made with the *Spitzer* Space Telescope, which is operated by the Jet Propulsion Laboratory, California Institute of Technology under a contract with NASA. Also based on observations made with ESO Telescopes at the La Silla Paranal Observatory under programme IDs 080.C-0587(A), 276.D-5014(A), 079.C-0683(B) and 080.C-0587(B). This research has made use of NASA's Astrophysics Data System Bibliographic Services and the models hosted by Pierre Bergeron here: http://www.astro.umontreal.ca/∼bergeron/CoolingModels.

REFERENCES

Anderson D. R. et al., 2011, ApJ, 726, L19
Baulch D. et al., 1994, J. Phys. Chem. Ref. Data, 23, 847
Beatty T. G. et al., 2014, ApJ, 783, 112
Beuermann K. et al., 2013, A&A, 558, A96
Burleigh M. R., Hogan E., Dobbie P. D., Napiwotzki R., Maxted P. F. L., 2006, MNRAS, 373, L55
Burleigh M. R. et al., 2011, in Schuh S., Drechsel H., Heber U., eds, AIP Conf. Proc. Vol. 1331, Planetary Systems Beyond the Main Sequence. Am. Inst. Phys., New York, p. 262
Casewell S. L. et al., 2012, ApJ, 759, L34
Casewell S. L., Burleigh M. R., Lawrie K. A., Maxted P. F. L., Dobbie P. D., Napiwotzki R., 2013, Mem. Soc. Astron. Ital., 84, 1022
Cooper C. S., Showman A. P., 2005, ApJ, 629, L45
Cushing M. C., Rayner J. T., Vacca W. D., 2005, ApJ, 623, 1115
Cutri R. M. et al., 2003, 2MASS All Sky Catalog of Point Sources
Dekker H., D'Odorico S., Kaufer A., Delabre B., Kotzlowski H., 2000, in Iye M., Moorwood A. F., eds, Proc. SPIE Conf. Ser. Vol. 4008, Optical and IR Telescope Instrumentation and Detectors. SPIE, Bellingham, p. 534
Dobbie P. D., Burleigh M. R., Levan A. J., Barstow M. A., Napiwotzki R., Hubeny I., 2005, A&A, 439, 1159
Draine B. T., 1978, ApJS, 36, 595
Drossart P. et al., 1989, Nature, 340, 539
Farihi J., Christopher M., 2004, AJ, 128, 1868
Fazio G. G. et al., 2004, ApJS, 154, 10
Field G. B., Somerville W. B., Dressler K., 1966, ARA&A, 4, 207

Fortney J. J., Marley M. S., Lodders K., Saumon D., Freedman R., 2005, ApJ, 627, L69
Fortney J. J., Cooper C. S., Showman A. P., Marley M. S., Freedman R. S., 2006, ApJ, 652, 746
Fortney J. J., Lodders K., Marley M. S., Freedman R. S., 2008, ApJ, 678, 1419
France K. et al., 2013, ApJ, 763, 149
Geballe T. R., Jagod M.-F., Oka T., 1993, ApJ, 408, L109
Goto M., Geballe T. R., McCall B. J., Usuda T., Suto H., Terada H., Kobayashi N., Oka T., 2005, ApJ, 629, 865
Hebb L. et al., 2009, ApJ, 693, 1920
Hill C., Yurchenko S. N., Tennyson J., 2013, Icarus, 226, 1673
Holberg J. B., Bergeron P., 2006, AJ, 132, 1221
Hubeny I., 1988, Comput. Phys. Commun., 52, 103
Hubeny I., Lanz T., 1995, ApJ, 439, 875
Hubeny I., Lanz T., 2001, TLUSTY. Available at http://nova.astro.umd.edu/
Hubeny I., Burrows A., Sudarsky D., 2003, ApJ, 594, 1011
Knutson H. A. et al., 2012, ApJ, 754, 22
Koskinen T. T., Aylward A. D., Smith C. G. A., Miller S., 2007, ApJ, 661, 515
Kowalski P. M., Saumon D., 2006, ApJ, 651, L137
Lammer H., Selsis F., Ribas I., Guinan E. F., Bauer S. J., Weiss W. W., 2003, ApJ, 598, L121
Lee H.-H., Herbst E., Pineau des Forets G., Roueff E., Le Bourlot J., 1996, A&A, 311, 690
Madhusudhan N. et al., 2011, Nature, 469, 64
Marley M. S., Gelino C., Stephens D., Lunine J. I., Freedman R., 1999, ApJ, 513, 879
Marley M. S., Seager S., Saumon D., Lodders K., Ackerman A. S., Freedman R. S., Fan X., 2002, ApJ, 568, 335
Maxted P. F. L., Napiwotzki R., Dobbie P. D., Burleigh M. R., 2006, Nature, 442, 543
Melin H., Miller S., Stallard T., Grodent D., 2005, Icarus, 178, 97
Miller S. et al., 2000, Phil. Trans. R. Soc. A, 358, 2485
Moorwood A., Cuby J.-G., Lidman C., 1998, The Messenger, 91, 9
Naylor T., 1998, MNRAS, 296, 339
Neale L., Miller S., Tennyson J., 1996, ApJ, 464, 516
Rimmer P. B., Helling C., Bilger C., 2014, Int. J. Astrobiol., 13, 173
Sing D. K. et al., 2013, MNRAS, 436, 2956
Steele P. R. et al., 2013, MNRAS, 429, 3492
Sternberg A., Dalgarno A., 1989, ApJ, 338, 197
Tennyson J., Yurchenko S. N., 2012, MNRAS, 425, 21
Trafton L. M., Geballe T. R., Miller S., Tennyson J., Ballester G. E., 1993, ApJ, 405, 761
Tremblay P.-E., Bergeron P., Gianninas A., 2011, ApJ, 730, 128
Yelle R. V., 2004, Icarus, 170, 167
Zahnle K., Marley M. S., Fortney J. J., 2009, preprint (arXiv:0911.0728)

This paper has been typeset from a TEX/LATEX file prepared by the author.